

Advanced separated spatial representations for hardly separable domains[☆]

Chady Ghnatios^{a,*}, Emmanuelle Abisset^b, Amine Ammar^c, Elías Cueto^d,
Jean-Louis Duval^e, Francisco Chinesta^f

^a*Norte Dame University-Louaize, Mechanical engineering department, Zouk Mosbeh, Lebanon*

^b*ESI Chair and I2M Lab, Arts et Métiers ParisTech Centre de Bordeaux-Talence, Esplanade des Arts et Métiers, 33400 Talence, France*

^c*LAMPA, ENSAM Angers, 2 Boulevard du Ronceray, BP 93525, 49035 Angers Cedex 01, France*

^d*Aragon Institute of Engineering Research (I3A), Universidad de Zaragoza. Maria de Luna 3, E-50018 Zaragoza, Spain*

^e*ESI GROUP. 3bis rue Saarinen, 94528 Rungis CEDEX, France*

^f*ESI Chair and PIMM Lab, Arts et Métiers ParisTech, 155 Boulevard de l'Hôpital. 75013 Paris, France*

Abstract

This work aims at proposing a new procedure for parametric problems whose separated representation has been considered difficult, or whose SVD compression impacted the results in terms of performance and accuracy. The proposed technique achieves a fully separated representation for layered domains with interfaces exhibiting waviness or—more generally—deviating from planar surfaces, parallel to the coordinate plane. This will make possible a simple separated representation, equivalent to others, already analyzed in some of our former works. To prove the potentialities of the proposed ap-

[☆]This work has been supported by the Spanish Ministry of Economy and Competitiveness through Grant number DPI2015-72365-EXP and by the Regional Government of Aragon and the European Social Fund, research group T24 17R.

*Corresponding author

Email addresses: `cghnatios@ndu.edu.lb` (Chady Ghnatios),
`Emmanuelle.Abisset-Chavanne@ensam.eu` (Emmanuelle Abisset),
`Amine.AMMAR@ensam.eu` (Amine Ammar), `ecueto@unizar.es` (Elías Cueto),
`jean-louis.duval@esi-group.com` (Jean-Louis Duval),
`francisco.chinesta@ensam.eu` (Francisco Chinesta)

proach, two benchmarks will be addressed, one of them involving an efficient space-time separated representation achieved by considering the same rationale.

Keywords: PGD, Space separated representation, Parametric modeling.

1. Introduction

When looking for an approximation of the solution $u(\mathbf{x}, t)$ of a given PDE, here assumed, without loss of generality, to be scalar and linear, the standard finite element method considers the approximation

$$u(\mathbf{x}, t) = \sum_{i=1}^{\mathbf{N}} U_i(t) N_i(\mathbf{x}), \quad (1)$$

where U_i denotes the value of the unknown field at node \mathbf{X}_i and $N_i(\mathbf{x})$ represents the so-called shape function associated to the i -th node. Here \mathbf{N} refers to the number of nodes employed to approximate the field u in the domain Ω in which the physical problem is defined.

This approximation results in an algebraic problem of size \mathbf{N} in the linear case, or the iterative solution of many of them in the general transient and nonlinear case. In order to alleviate the computational cost, model order reduction techniques were proposed and are nowadays intensively used.

In the framework of POD-based model order reduction [9], a learning stage allows extracting the significant modes $\phi_i(\mathbf{x})$ that best approximate the solution. In many cases, a reduced number of modes \mathbf{R} ($\mathbf{R} \ll \mathbf{N}$) suffice to approximate the solution of problems similar to the one that served to extract the modes in the learning stage.

Thus, the solution $u(\mathbf{x}, t)$ is projected onto the reduced basis composed of functions $\{\phi_1(\mathbf{x}), \dots, \phi_{\mathbf{R}}(\mathbf{x})\}$, according to

$$u(\mathbf{x}, t) \approx \sum_{i=1}^{\mathbf{R}} \xi_i(t) \phi_i(\mathbf{x}), \quad (2)$$

that now requires the solution of linear systems of size \mathbf{R} instead the ones of size \mathbf{N} characteristic of finite element solutions. This often allows us to obtain impressive computing time savings.

Approximations (1) or (2) imply a finite sum of time-dependent coefficients and space functions. The last are assumed known: they consist of the usual finite element shape functions or the modes extracted by applying the POD. A generalization of this procedure could consist on assuming that space functions are also unknown and therefore to compute both, time and space functions, on the fly [19]. Thus, this approximation reads

$$u(\mathbf{x}, t) \approx \sum_{i=1}^{\mathbf{M}} T_i(t) X_i(\mathbf{x}). \quad (3)$$

Since both functions involved in approximation (3) are unknown, the problem solution becomes nonlinear, and its solution requires an appropriate linearization strategy. The interested reader can refer to [2, 7, 11, 20, 23, 25, 26] and the references therein for practical details on the computer implementation of separated representations.

Expression (3) evidences that the solution procedure requires the solution of about \mathbf{M} problems, with $\mathbf{M} \ll \mathbf{N}$ and $\mathbf{M} \sim \mathbf{R}$ (slightly more, in fact, because of the nonlinearity induced by separated representations) involving the space coordinates (in general three-dimensional and whose associated discrete systems are of size \mathbf{N}) to compute the space functions $X_i(\mathbf{x})$ and about \mathbf{M} one-dimensional problems to calculate the time functions $T_i(t)$. Due to the fact that the computing cost related to the solution of 1D problems is negligible with respect to the solution of 3D problems, the resulting computational complexity reduces drastically, scaling with \mathbf{M} instead of \mathbf{P} (here, \mathbf{P} represents the number of time steps considered in the time domain discretization and that corresponds with the complexity of standard incremental time-integration

techniques).

Another step forward consisted in assuming model parameters as extra-coordinates. Thus, space-time-parameters separated representations allowed constructing the so-called computational vademecums (also known as abacus, virtual charts, nomograms, ...) efficiently employed for multiple purposes: simulation, optimization, inverse analysis, uncertainty propagation and simulation-based control, all them under real-time constraints [6, 9]. When the unknown field involves space, time and a series of parameters μ_1, \dots, μ_q , its associated separated representation reads

$$u(\mathbf{x}, t, \mu_1, \dots, \mu_q) \approx \sum_{i=1}^M X_i(\mathbf{x})T_i(t) \prod_{j=1}^q M_i^j(\mu_j). \quad (4)$$

1.1. Space separation

The separation of space coordinates was also intensively considered in our former works referred later, as well as in other references, see, for instance, [10] and the references therein. Space separation allowed addressing multi-physics problems defined in degenerated geometries in which at least one of its dimensions results to be much smaller than the other ones (e.g. beams, plates, shells, laminates) or processes involving additive layers (e.g., automated tape placement, 3D printing, or additive manufacturing). Thus, if domain Ω can be decomposed as $\Omega = \Omega_x \times \Omega_y \times \Omega_z$, the solution $u(x, y, z)$ could be approximated by using the separated representation

$$u(x, y, z) \approx \sum_{i=1}^M X_i(x)Y_i(y)Z_i(z), \quad (5)$$

that allows calculating the 3D solution from a sequence of 1D problems.

For some geometries, as the ones concerning plates or shells, in-plane-out-of-plane separated representations become specially appealing,

$$u(x, y, z) \approx \sum_{i=1}^M X_i(x, y)Z_i(z), \quad (6)$$

where the 3D complexity is reduced to a 2D complexity, related to the calculation of in-plane functions $X_i(x, y)$.

As discussed in [9], the cost savings provided by the use of these separated representations are potentially impressive when the spatial domain is fully separable. Indeed, the complexity of the simulation now scales with the one-dimensional meshes used to solve the BVP's in Ω_x , Ω_y and Ω_z , associated to the computation of functions $X_i(x)$, $Y_i(y)$ and $Z_i(z)$ or with the two-dimensional ones associated with the calculation of functions $X_i(x, y)$ in the case of in-plane-out-of-plane separated representations [7].

When the domain is not intrinsically separable or, in other words, expressible from a direct cartesian product, fully separated representations require the use appropriate geometrical mappings [1, 10] or the immersion of the non-separable domain onto a fully separable one [15, 17].

In-plane/out-of-plane separated representations are particularly useful for addressing the solution of problems defined in plate and shell geometries, [3] and [4] respectively, or extruded domains [21]. A parametric 3D elastic solution of beams involved in frame structures was proposed in [5]. The same approach was extensively considered in structural plate and shell models in [12, 28–32] and [24].

Space separated representations were enriched with discontinuous functions for representing cracks in [16], delamination [22] and thermal contact resistances in [8]. The in-plane/out-of-plane decomposition was then extended to many other physics like squeeze flows of Newtonian and non-Newtonian fluids in layered domains in [14] or electromagnetism [27].

1.2. Paper outline

The present paper aims to propose a new simple procedure for treating, in a fully separated representation manner, problems in which the expres-

sion of the parametric dependency in a separated form was considered difficult, or where the separated representation performed by invoking SVD-like techniques had a significant impact in the performance and efficiency of the resulting numerical procedures.

After the just addressed introduction on separated representations, with special emphasis in those involving space coordinates, the next section will introduce the main idea of the present work. Namely, a very efficient geometrical mapping leading to a separable description of the problem. Then, in Section 3, the proposed approach is applied to the solution of thermal problems defined in thin domains, but in which the material conductivity has not a compact separated representation. Section 4 addresses the issue of 1D thermal problems containing an inclusion of a different thermal conductivity and whose position in the domain is assumed to be the model parameter. Consequently, the temperature field for any position of the inclusion is found. The paper finishes by summarizing the most valuable conclusions.

2. Domain mapping

We introduce the proposed methodology, for the sake of simplicity and without loss of generality, by making use of a two-dimensional heat transfer problem. Thus, we consider the temperature field $u(\mathbf{x})$, $\mathbf{x} = (x, y)$, defined in a thin domain $\Omega = (0, L) \times (0, H)$, with $H \ll L$, where a non-planar internal boundary (as the one sketched in Fig. 1) separates the upper domain Ω_u , with thermal conductivity K_u , and the bottom domain, Ω_b , with conductivity K_b . This boundary is defined by a function $h(x)$.

The temperature field is assumed to be the solution of the steady-state heat transfer problem defined in Ω , whose weak form reads

$$\int_{\Omega} K(\mathbf{x}) \nabla u^* \cdot \nabla u \, d\mathbf{x} = 0, \quad (7)$$

with $u \in H^1(\Omega)$ space and $u^* \in H_0^1(\Omega)$. The problem is subjected to the boundary conditions

$$\left\{ \begin{array}{l} \frac{\partial u(x,y)}{\partial x} \Big|_{x=0} = 0, \\ \frac{\partial u(x,y)}{\partial x} \Big|_{x=L} = 0, \\ u(x, 0) = 0, \\ u(x, H) = u_g, \end{array} \right. \quad (8)$$

where u_g denotes the prescribed, temperature on the top surface.

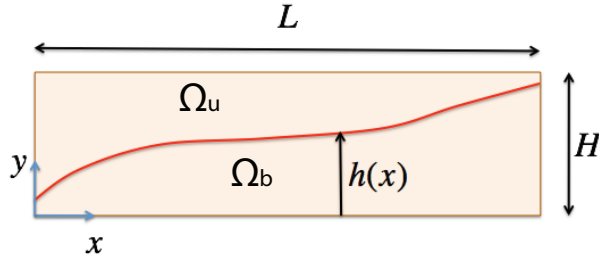


Figure 1: Domain containing a nonplanar internal boundary

Because of the small domain thickness, i.e., $H \ll L$, standard mesh-based discretization techniques fail due to the excessive number of degrees of freedom due to the domain degeneracy, i.e. the very different characteristic dimensions, with the thickness dimension orders of magnitude smaller than the others. Those based on the use of separated representations

$$u(x, y) \approx \sum_{i=1}^M X_i(x)Y_i(y), \quad (9)$$

are faced to the difficulties relative to the presence of the non-planar boundary, that implies a hardly separable conductivity field, that as discussed below

needs too many modes, M , to converge, that is, for reaching a residual small enough [7].

Of course, conductivity can always be separated by invoking, for instance, the singular value decomposition (SVD), i.e., by expressing the conductivity as

$$K(x, y) \approx \sum_{k=1}^L F_k(x)G_k(y). \quad (10)$$

In the case of a planar boundary $\Gamma = \bar{\Omega}_u \cap \bar{\Omega}_b$, characterized by $h(x) = h$, with $0 < h < H$, a single term suffices for separating the conductivity, i.e.,

$$K^p(x, y) = F^p(x)G^p(y), \quad (11)$$

where the superscript $(\bullet)^p$ refers to the planar interface configuration, $F^p(x) = 1$ and $G^p(x)$ is defined by

$$G^p(y) = K_u - (K_u - K_b)\chi(y), \quad (12)$$

with

$$\chi(y) = \begin{cases} 1 & y < h \\ 0 & y \geq h \end{cases}. \quad (13)$$

However, when internal boundaries deviate from the planar configuration, the number of modes K increases prohibitively, and with it the operators involved in the weak form (7). Thus, both the performance and the efficiency of the solver are seriously compromised.

In order to circumvent this issue, we define two mappings transforming Ω_u and Ω_b into two rectangular domains, noted respectively \mathcal{R}_u and \mathcal{R}_b .

1. *Mapping Ω_b into \mathcal{R}_b .* The first mapping with $\mathbf{r} = (r, s) \in \mathcal{R}_b = (0, L) \times (0, 1)$ reads

$$\begin{cases} x = r, \\ y = s h(r), \end{cases} \quad (14)$$

or, equivalently,

$$\begin{cases} r = x, \\ s = \frac{y}{h(x)}. \end{cases} \quad (15)$$

The components of the Jacobian matrix \mathbf{J}_b result

$$\begin{cases} \frac{\partial x}{\partial r} = 1, \\ \frac{\partial x}{\partial s} = 0, \\ \frac{\partial y}{\partial r} = s h'(r), \\ \frac{\partial y}{\partial s} = h(r), \end{cases} \quad (16)$$

that allows transforming the differential operators involved in the weak form (7), $\nabla = (\frac{\partial}{\partial x}, \frac{\partial}{\partial y})^T$ as

$$\begin{cases} \frac{\partial \bullet}{\partial x} = \frac{\partial \bullet}{\partial r} \frac{\partial r}{\partial x} + \frac{\partial \bullet}{\partial s} \frac{\partial s}{\partial x} = \frac{\partial \bullet}{\partial r} - \frac{\partial \bullet}{\partial s} s \frac{h'(r)}{h(r)}, \\ \frac{\partial \bullet}{\partial y} = \frac{\partial \bullet}{\partial r} \frac{\partial r}{\partial y} + \frac{\partial \bullet}{\partial s} \frac{\partial s}{\partial y} = \frac{\partial \bullet}{\partial s} \frac{1}{h(r)}, \end{cases} \quad (17)$$

that, together with

$$d\mathbf{x} = \det(\mathbf{J}_b) d\mathbf{r} = h(r) d\mathbf{r}, \quad (18)$$

allows rewriting the weak form (7). For this purpose, we define matrix \mathbf{B}_b

$$\mathbf{B}_b = \begin{pmatrix} 1 & -s \frac{h'(r)}{h(r)} \\ 0 & \frac{1}{h(r)} \end{pmatrix}, \quad (19)$$

and the gradient operator $\nabla_r = (\frac{\partial}{\partial r}, \frac{\partial}{\partial s})^T$, such that

$$\nabla \bullet = \mathbf{B}_b \nabla_r \bullet, \quad (20)$$

that allows writing the weak form as

$$\int_{\mathcal{R}_b} K_b (\nabla_r u^*)^T \mathbf{B}_b^T \mathbf{B}_b \nabla_r u \det(\mathbf{J}_b) d\mathbf{r} = 0. \quad (21)$$

2. *Mapping Ω_u into \mathcal{R}_u .* Equivalently, for Ω_u we define

$$\begin{cases} x = r, \\ y = (s - 1)(H - h(r)) + h(r), \end{cases} \quad (22)$$

with $(r, s) \in \mathcal{R}_u = (0, L) \times (1, 2)$.

The gradient operator and the Jacobian are then calculated for this mapping following the same rationale considered in the previous approach. The final weak form in \mathcal{R}_u reads

$$\int_{\mathcal{R}_u} K_u (\nabla_r u^*)^T \mathbf{B}_u^T \mathbf{B}_u \nabla_r u \det(\mathbf{J}_u) d\mathbf{r} = 0, \quad (23)$$

where \mathbf{B}_u is now given by

$$\mathbf{B}_u = \begin{pmatrix} 1 & \frac{h'(s-2)}{H-h} \\ 0 & \frac{1}{H-h} \end{pmatrix}. \quad (24)$$

By defining the characteristic functions of both subdomains, $\chi_u(\mathbf{r})$ and $\chi_b(\mathbf{r})$,

$$\chi_u(\mathbf{r}) = \begin{cases} 1 & \text{if } s \geq 1, \\ 0 & \text{if } s < 1, \end{cases} \quad (25)$$

and

$$\chi_b(\mathbf{r}) = \begin{cases} 1 & \text{if } s < 1, \\ 0 & \text{if } s \geq 1. \end{cases} \quad (26)$$

By using the notations

$$\begin{cases} K(\mathbf{r}) = \chi_u(\mathbf{r})K_u + \chi_b(\mathbf{r})K_b, \\ \mathbf{B}(\mathbf{r}) = \chi_u(\mathbf{r})\mathbf{B}_u(\mathbf{r}) + \chi_b(\mathbf{r})\mathbf{B}_b(\mathbf{r}), \\ \det(\mathbf{J}(\mathbf{r})) = \chi_u(\mathbf{r})\det(\mathbf{J}_u(\mathbf{r})) + \chi_b(\mathbf{r})\det(\mathbf{J}_b(\mathbf{r})), \end{cases} \quad (27)$$

the weak form in $\mathcal{R} = \mathcal{R}_u \cup \mathcal{R}_b$ reads

$$\int_{\mathcal{R}} K(\mathbf{r}) (\nabla_r u^*)^T \mathbf{B}^T(\mathbf{r}) \mathbf{B}(\mathbf{r}) \nabla_r u \det(\mathbf{J}(\mathbf{r})) d\mathbf{r} = 0. \quad (28)$$

Now, $u(r, s)$ is approximated in the separated form

$$u(r, s) \approx \sum_{i=1}^M R_i(r) S_i(s). \quad (29)$$

The problem can therefore be solved in a separated representation as a sequence of problems in the r and s coordinate domains, by using the standard PGD procedure (see [7] for more details).

The main and major advantage of the proposed mapping is its capacity for preserving the separated form of Jacobians.

3. Numerical examples

This section addresses different case studies: 2D and 3D domains with non-separable interfaces, a parametric problem involving an inclusion and finally the problem of a thermal source moving along a one-dimensional domain. In all the numerical examples which follow, each domain is discretized with a uniform mesh.

3.1. 2D domains with non separable interface

In this section the applied boundary conditions (in the sequel all units are assumed to be in the metric system) read:

$$\begin{cases} u(x, y = 0) = 0, \\ u(x, y = H) = 25, \\ \frac{\partial u(x, y)}{\partial y} \Big|_{x=0} = 0, \\ \frac{\partial u(x, y)}{\partial y} \Big|_{x=L} = 0. \end{cases} \quad (30)$$

In what follows, we analyze two kinds of non-separable boundaries.

3.1.1. Parabolic interphase

In this first numerical example we consider an extremely thin rectangular domain $\Omega = (0, 1) \times (0, 10^{-3})$, i.e., $H = 10^{-3}$ and $L = 1$, with the internal boundary $h(x)$ defined by the parabolic curve

$$h(x) = \frac{H}{2} (0.5 + 2x - x^2). \quad (31)$$

This boundary defines two domains with different thermal conductivities: the upper domain has a conductivity $K_u = 10$, whereas the bottom one has a conductivity $K_b = 1$. The interface $h(x)$ is depicted in Fig. 2. The PGD solution is achieved in 0.2 seconds on a standard laptop using 100 nodes in the r -mesh and 1000 nodes in the s -mesh. Note that this resolution is equivalent to the use of $2 \cdot 10^5$ finite element degrees of freedom.

The solution in the (r, s) domain is shown in Fig. 3, whereas the one in the actual (x, y) domain is depicted in Fig. 4. The PGD solution involves $M = 6$ terms, that allowed a residual reduction of 9 orders of magnitude, i.e., a reduction factor of 10^{-9} .

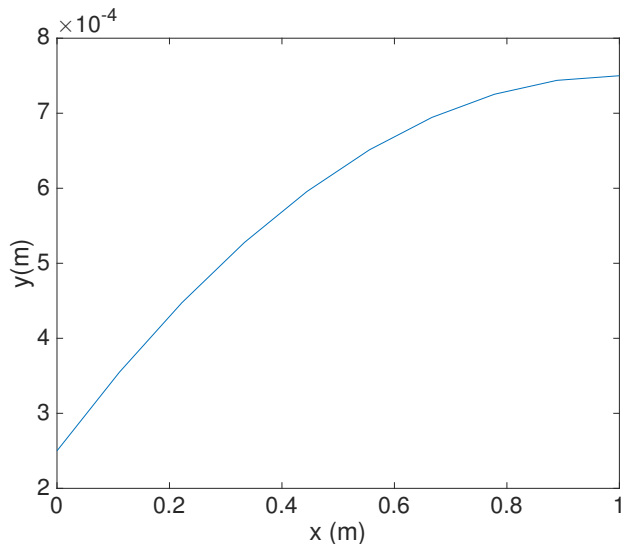


Figure 2: Interface in Ω defining the top and bottom domains Ω_u and Ω_b

When expressing the conductivity in a separated form according to Eq. (10) by invoking the singular value decomposition, $K = 96$ modes are needed for a reduction of six orders of magnitude of the associated eigenvalues. The solution using that K -mode separated representation of the thermal conductivity requires a non negligible effort, first for performing the SVD and then

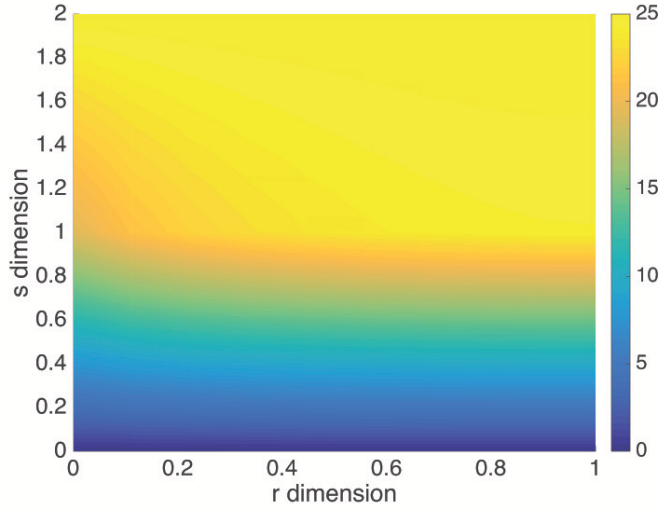


Figure 3: Solution in the reference domain $\mathcal{R} = \mathcal{R}_u \cup \mathcal{R}_b$.

for constructing the separated representation of the temperature. In the last, more than 50 temperature modes (i.e., $M > 50$) were required to reach an acceptable accuracy, needing more than half an hour of calculation.

It is worth mentioning that, when using the approach based on the separation of the thermal conductivity, the usual separated representation constructor, see [7], that proceeds by computing rank-one updates, hardly converged, and each new mode produced only a very slight reduction of the residual.

3.1.2. Wavy boundary

In this second example the boundary $h(x)$ is defined from

$$h(x) = \frac{H}{4} \sin(4x\pi) + \frac{H}{2}. \quad (32)$$

Meshes and model parameters are the same that the ones considered in the previous case study. Despite of poor separability of the thermal conductivity field, again by using the mappings discussed in Section 2, the solution contained only $M = 6$ modes. It was obtained in 0.36 seconds, with a similar residual reduction factor (10^{-9}).

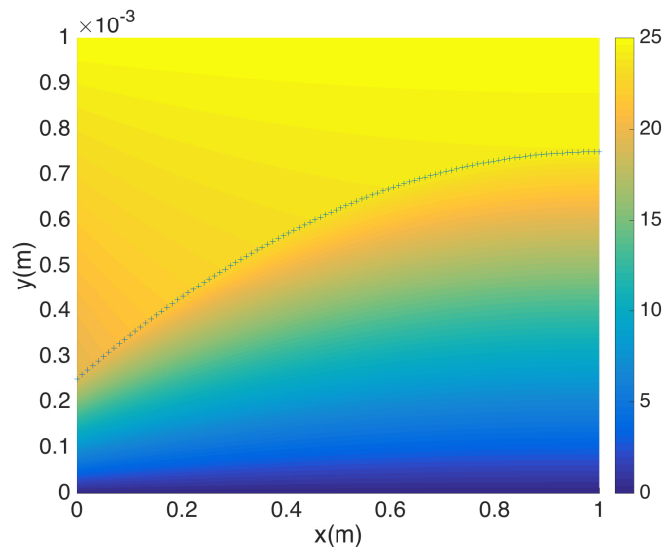


Figure 4: Solution in the actual domain $\Omega = \Omega_u \cup \Omega_b$ with the interface location highlighted.

The solutions in the reference and actual domains, \mathcal{R} and Ω , are depicted respectively in Figs. 5 and 6. Again, the interface location is highlighted. When using a SVD-based separated representation of the conductivity field, the solver hardly converges, and every new mode reduced very slightly the residual. Consequently, the calculation required again more than half an hour.

3.2. Three-dimensional layered domain with an inclined flat interface

In this section the procedure described in Section 2 is extended to the 3D case considering the domain sketched in Fig. 7, with $\Omega = (0, L_x) \times (0, H) \times (0, L_z)$.

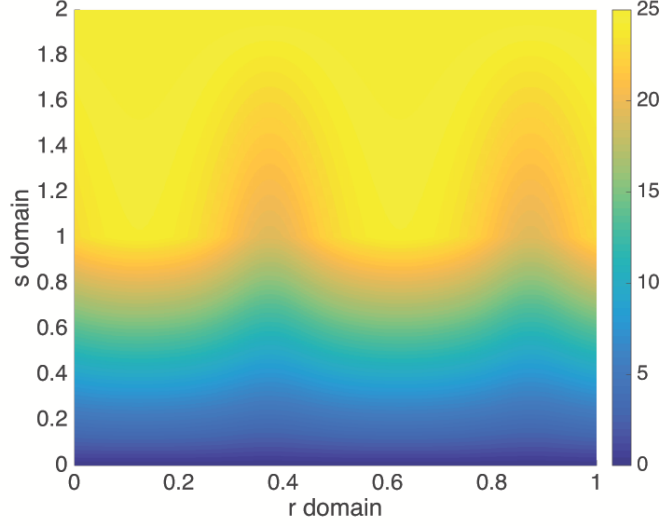


Figure 5: Solution in the reference domain $\mathcal{R} = \mathcal{R}_u \cup \mathcal{R}_b$.

Now the mapping $(r, s, t) \rightarrow (x, y, z)$ reads:

$$\text{for } s \in (0, 1) \begin{cases} x = r, \\ y = s h(x, z), \\ z = t, \end{cases} \quad (33)$$

$$\text{for } s \in (1, 2) \begin{cases} x = r, \\ y = (s - 1) (H - h(x, z)) + h(x, z), \\ z = t, \end{cases}$$

where $h(x, z)$ is given by

$$h(x, z) = (H/4) + (H/2) \frac{x}{L_x}. \quad (34)$$

The thermal problem is solved by prescribing temperatures at the top and bottom surfaces, $u(x, 0, z) = 0$ and $u(x, H, z) = 25$, while enforcing null heat fluxes on the lateral surfaces $x = 0$, $x = L_x$, $z = 0$ and $z = L_z$. The thermal conductivities of the subdomains located above and below the interface, K_u and K_b , are the same that the ones previously considered.

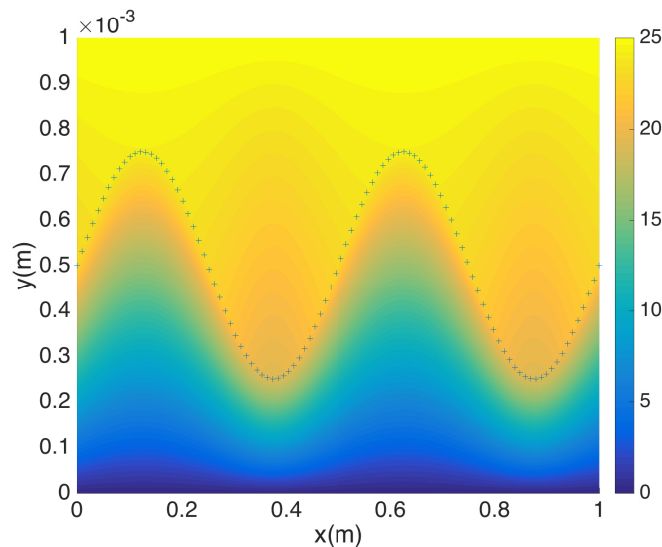


Figure 6: Solution in the actual domain $\Omega = \Omega_u \cup \Omega_b$ with the interface location highlighted.

Figure 8 depicts on the reference domain \mathcal{R} the solution on the domain cross section $t = L_z/2$, while Fig. 9 shows the solution at the corresponding cross section of the actual domain Ω . Figure 10 depicts the 3D plot of the solution on the actual 3D domain Ω .

The meshes considered in this simulation consisted of 100 nodes along the r - and t -coordinates, and 1000 along the thickness s , to reach a resolution equivalent to 10^7 finite element degrees of freedom. The most remarkable fact was that the calculation was accomplished in 3 seconds in a standard laptop, and that $M = 15$ modes were enough for reducing the residual in 8 orders of magnitude, that is, a reduction by factor of 10^{-8} .

When expressing the conductivity using both, an in-plane/out-of-plane separated form or a fully separated form, by invoking in both cases the SVD, the usual rank-one constructor [7] did not reach convergence after computing 100 modes (note that 15 modes were enough when using the procedure based on the mapping described in Section 2).

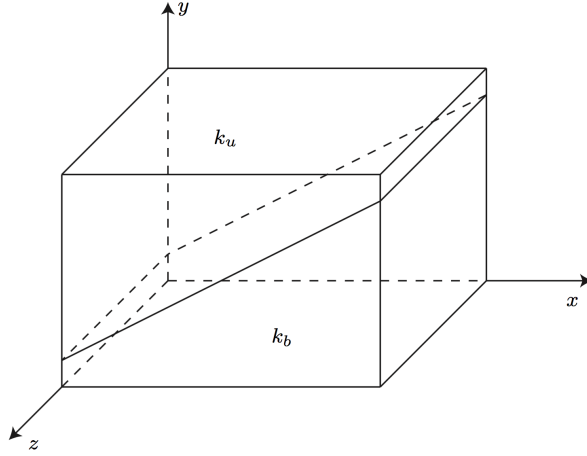


Figure 7: 3D case study involving a non-planar interface in the plate domain $1 \times 10^{-3} \times 1$ (units in meters).

3.3. Parametric inclusion

In this example we analyze an issue of major relevance, related to a thermal problem in a one-dimensional domain $x \in [0, L]$, with $L = 1$, assumed to be composed by a material of thermal conductivity $K_1 = 5$ that contains an inclusion of length $l = L/20$ and conductivity $K_2 = 1$ (IS units), with its central point located at position $X \in [0.035L, 0.965L]$.

The parametric temperature field is sought. In other words, we look for the expression of the temperature field for any possible position of the inclusion X , i.e., $u(x; X)$. Within the PGD rationale, the inclusion location X is considered as an extra-coordinate, so that the temperature field becomes two dimensional, i.e. $u(x, X)$, while the complexity due to the increase of dimensionality is compensated by the use of the separated representation.

The parametric weak form of the heat equation now reads

$$\int_{\Omega} \frac{\partial u^*}{\partial x} K(x; X) \frac{\partial u}{\partial x} dx = \int_{\Omega} u^* Q dx, \quad (35)$$

with Q the heat source term.

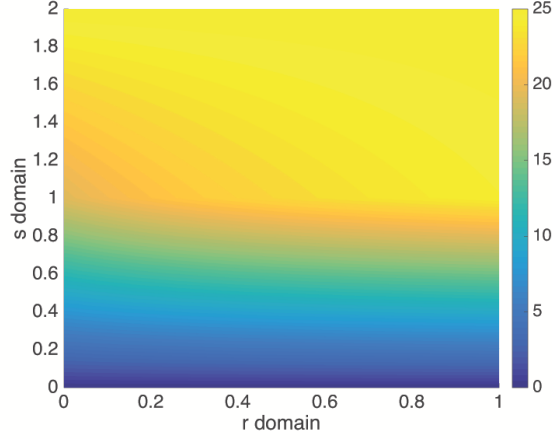


Figure 8: Temperature $u(r, s, L_z/2)$.

We consider the mapping:

$$\begin{aligned}
 s \in [0, 1] & \begin{cases} X = r, \\ x = sh_1(X) = sh_1(r), \end{cases} \\
 s \in [1, 2] & \begin{cases} X = r, \\ x = (s-1)l + h_1(X) = (s-1)l + h_1(r), \end{cases} \\
 s \in [2, 3] & \begin{cases} X = r, \\ x = (s-2)h_2(X) + l + h_1(X) = (s-2)h_2(r) + l + h_1(r), \end{cases}
 \end{aligned} \tag{36}$$

where $h_1(X)$ is the position of the inclusion left boundary, i.e. $h_1(X) = X - l/2$, l is the inclusion length and $h_2(X)$ the distance between the right boundary of the inclusion and the domain right boundary, i.e. $h_2(X) = L - X - l/2$. The mapping (36) is sketched in Fig. 11.

By using the expression of the Jacobian, the heat problem weak form (35) can be expressed in the reference (r, s) domain and discretized without major difficulties, thus leading the parametric solution in the separated form

$$u(r, s) \approx \sum_{i=1}^M R_i(r) S_i(s). \tag{37}$$

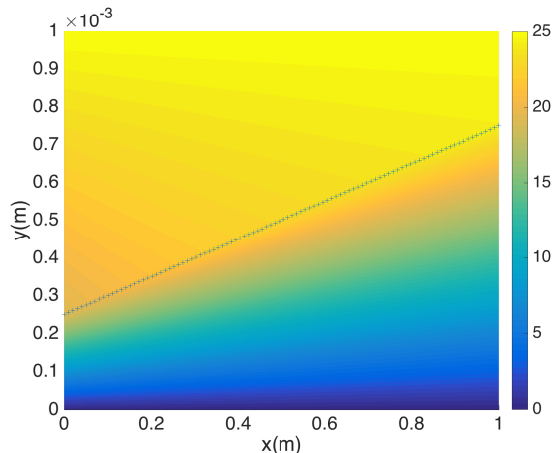


Figure 9: Temperature $u(x, y, L_z/2)$.

3.3.1. First numerical case

In this first numerical example we consider $Q = 50$ with the thermal conductivity $K(x; X)$ expressed form:

$$K(x; X) = \begin{cases} 5 & \text{if } x \in [X - l/2, X + l/2], \\ 1 & \text{if } x \in [0, X - l/2] \cup [X + l/2, L], \end{cases} \quad (38)$$

and homogeneous boundary conditions, $u(x = 0) = 0$ and $u(x = L) = 0$.

Meshes contained 1500 and 100 nodes along the s - and r -domains, respectively. The parametric solution $u(r, s)$, and consequently its counterpart $u(x, X)$, were obtained in less than 1s again by making use of a standard laptop, with a reduction factor of 30 with respect to the 100 1D calculations needed for computing the equivalent parametric temperature field, one for each of the 100 discrete positions of the inclusion. Of course, when increasing the problem dimensionality (2D or 3D) the computing time savings are much higher. The constructed separated representation involves $M = 10$ modes.

Figure 12 depicts the PGD solution of the problem while Fig. 13 illustrates the one related to the solution of the 100 1D problems. A maximum relative error of 0.7% was found. The maximum error localizes around the

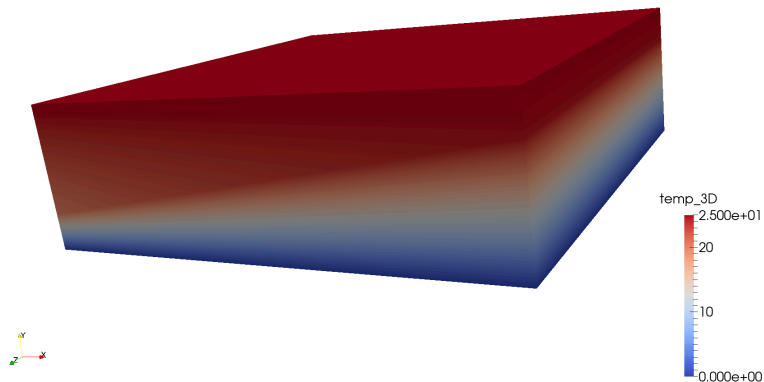


Figure 10: 3D solution representation in the plate domain of dimension $1 \times 10^{-3} \times 1 \text{ m}^3$.

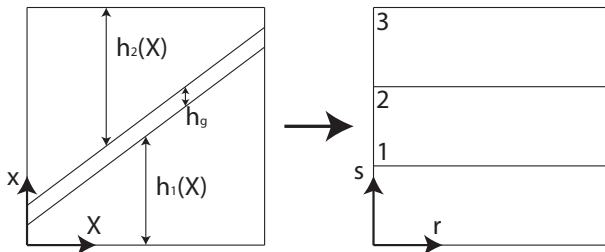


Figure 11: The geometrical transformation depicted in Eq.(36)

bottom left and top right corners, where the mapping exhibits the largest gradients.

It is worth noting, with respect to the discussion addressed in previous sections, that if we try, as discussed in [13], to proceed by separating the thermal conductivity $K(x, X)$ according to

$$K(x, X) \approx \sum_{i=1}^K F_i(x)G_i(X), \quad (39)$$

by invoking the SVD, the parametric solution $u(x, X)$ directly constructed in the domain Ω involves $M = 97$ modes, and requires 10 times more computing time.

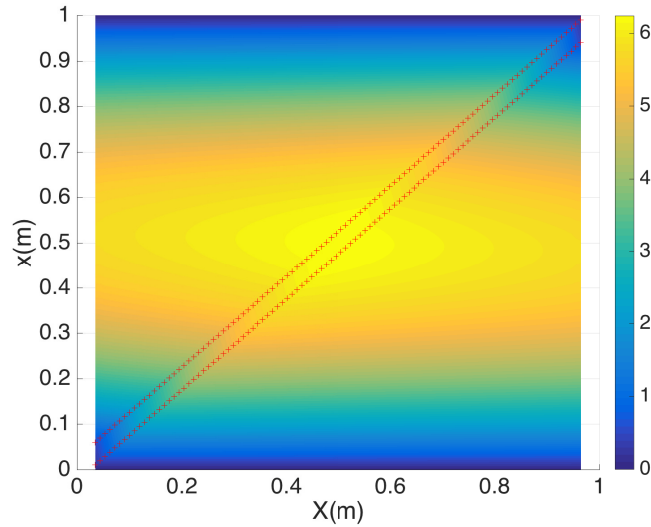


Figure 12: First numerical example: Parametric solution $u(x, X)$ computed by using the separated representation constructor operating on mapped domain \mathcal{R} .

3.3.2. Second numerical case

In order to better emphasizing the effect of the inclusion, we consider $Q = 0$, the thermal conductivity expressed now from

$$K(x; X) = \begin{cases} 1 & \text{if } x \in [X - l/2, X + l/2], \\ 5 & \text{if } x \in [0, X - l/2] \cup [X + l/2, L], \end{cases} \quad (40)$$

and the boundary conditions, $u(x = 0) = 0$ and $u(x = L) = 25$.

The computational performance is almost the same as the previous numerical example. Figure 14 depicts the PGD solution of the problem while Fig. 15 illustrates the one related to the solution of the 100 1D problems. Again a maximum relative error of 0.7% is found, in the regions where the mapping gradients are larger.

3.4. Thermal source moving along a one-dimensional domain

In this example, we consider $L = 1m$ and the thermal source location X defined in $X \in \Omega = [0.035L, 0.965L]$. X thus depends on the time from

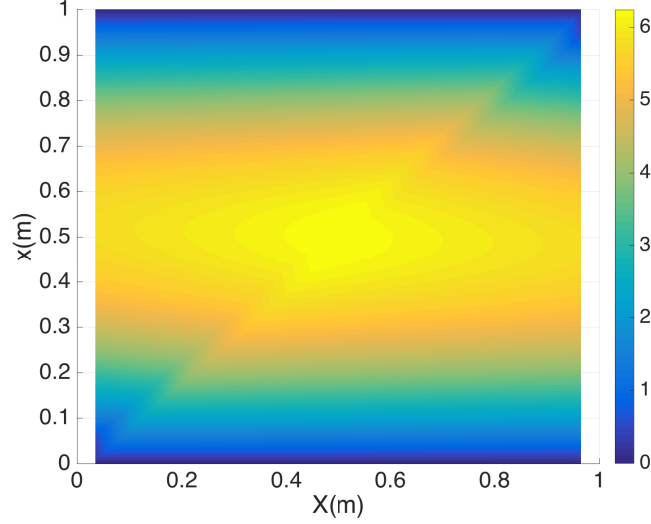


Figure 13: First numerical example: Solution for the different inclusion positions, $u(x; X_i)$, $i = 1, \dots, 100$.

$X = x_0 + \nu t$. In this example, the thermal source velocity ν corresponds to a movement from $X = 0.035L$ to $X = 0.965L$ in 1s., leading to $x_0 = 0.035$ and $\nu = 0.93$. The parametric weak form reads

$$\int_{\Omega \times \mathcal{I}} u^* \frac{\partial u}{\partial t} + \frac{\partial u^*}{\partial x} k \frac{\partial u}{\partial x} dx dt = \int_{\Omega \times \mathcal{I}} f(x, t) dx dt, \quad (41)$$

where \mathcal{I} represents the considered time interval.

The source location and the geometrical construction is depicted in Fig. 16. The relation between time t and source location X writes

$$t = \frac{(X - x_0)}{\nu}. \quad (42)$$

From Fig. 16, the heat source can be easily defined from:

$$\begin{cases} h_1(X) = X - \frac{h_g}{2}, \\ h_g(X) = \frac{L}{20}, \\ h_2(X) = L - \frac{h_g}{2} - X. \end{cases} \quad (43)$$

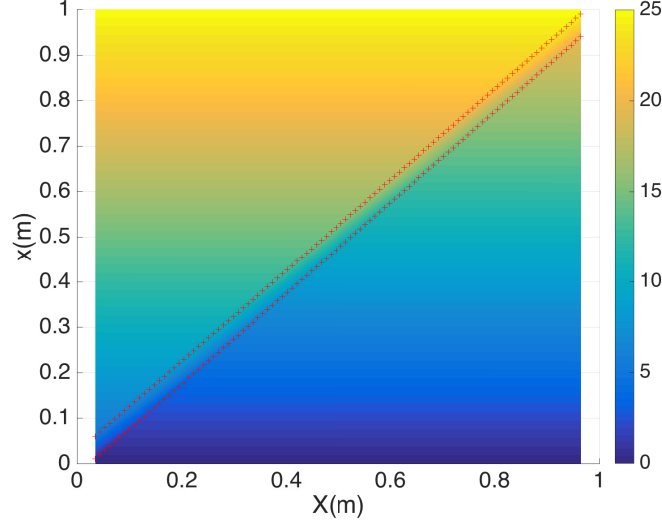


Figure 14: Second numerical example: Parametric solution $u(x, X)$ computed by using the separated representation constructor operating on mapped domain \mathcal{R} .

We define a new mapping:

$$\begin{aligned}
 \text{For } s \in [0, 1] & \begin{cases} X = x_0 + \nu t, \\ x = sh_1(X), \end{cases} \\
 \text{For } s \in [1, 2] & \begin{cases} X = x_0 + \nu t, \\ x = (s - 1)h_g + h_1(X), \end{cases} \\
 \text{For } s \in [2, 3] & \begin{cases} X = x_0 + \nu t, \\ x = (s - 2)h_2(X) + h_g + h_1(X), \end{cases}
 \end{aligned} \tag{44}$$

that allows transforming the problem weak form into the reference (physical) space (x, X) .

In the numerical solution, we assume the uniform source $f = 1$ defined between h_1 and h_2 as depicted in Fig. 16. The heat source term $f(x, t)$ in the actual domain is shown in Fig. 17, associated to the one in the reference domain depicted in Fig. 18 for the apparent source intensity $f_{\text{app}} = f \frac{h_g}{\nu}$. The considered mesh consisted of 600 nodes along the s coordinate and 300

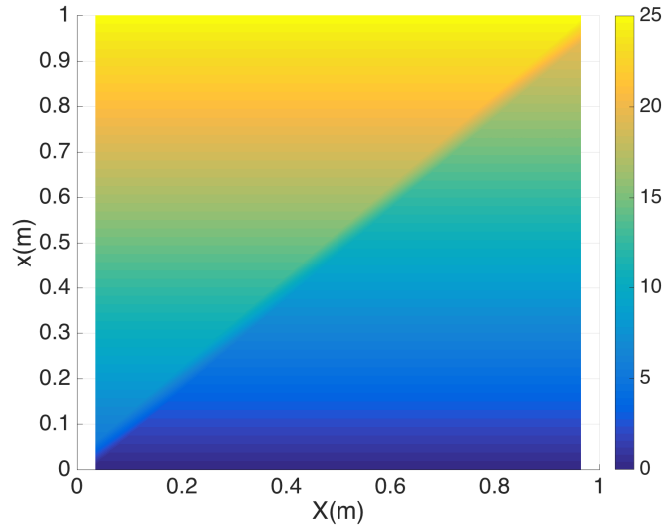


Figure 15: Second numerical example: Solution for the different inclusion positions, $u(x; X_i)$, $i = 1, \dots, 100$.

in the X domain. The PGD solution converged after 1.18s and consisted of 15 modes, reducing the residual more than 3 orders of magnitude. The solution in the reference domain (X, s) is shown in Fig. 19, whereas the one in the actual domain (x, t) is depicted in Fig. 20.

The same problem was solved using the standard PGD procedure. First the source term was expressed in a space-time separated form by invoking the SVD. Because its poor separability, many modes were required, with the eigenvalues involved in the SVD decomposition decreasing very slowly. Then, the standard rank-one greedy algorithm computed the temperature solution. However, its poor separability required again more than 100 modes and more than 50 seconds calculation to find a solution that exhibits small oscillations.

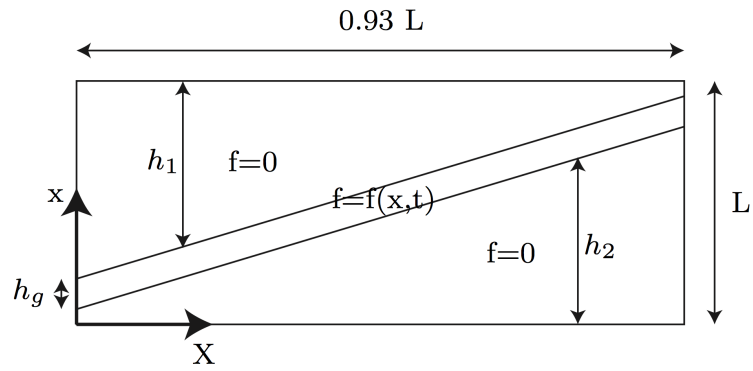


Figure 16: Heat source in the (x, X) physical space

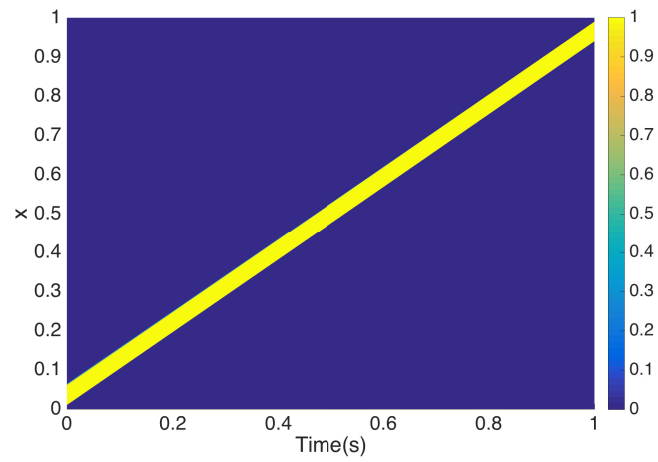


Figure 17: The heat source in the actual domain (X, s)

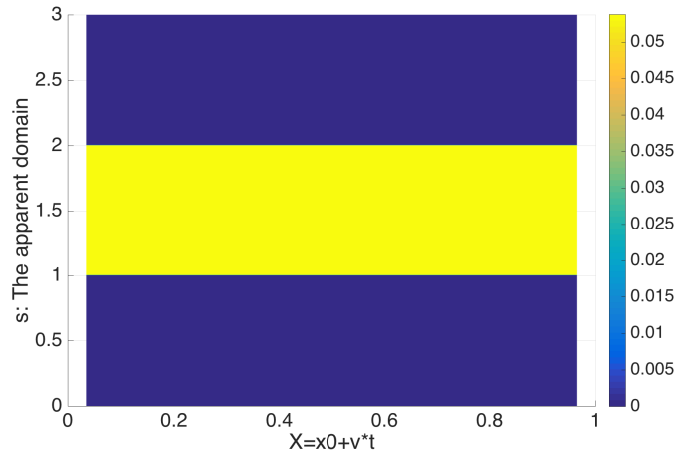


Figure 18: The heat source in the reference domain (s, t)

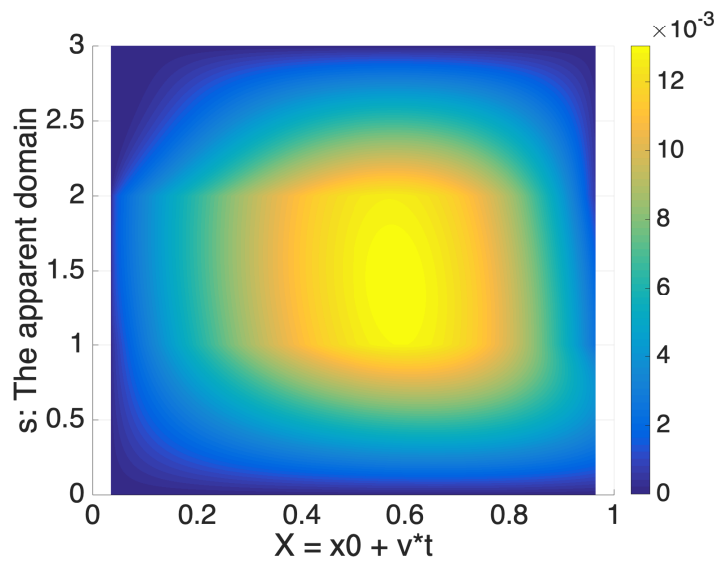


Figure 19: Temperature in the reference domain (X, s)

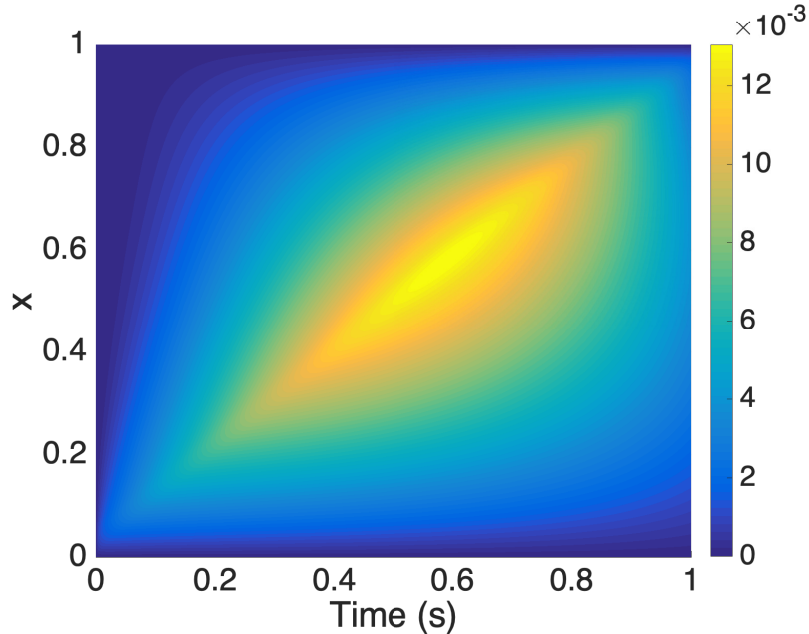


Figure 20: Temperature in the actual domain (x, t)

4. Conclusions

In this paper we addressed the space separation in layered domains Ω where interfaces are not planar (or, even being planar, are not parallel with respect to the in-plane-coordinate). In these circumstances, former works stressed that space-separated representations lose their expected effectiveness. In fact, that conclusion was derived from the fact that these geometries involved too many terms in the material property-separated representations when invoking the SVD or its high order counterpart, the so-called HOSVD [18]. In these circumstances, the separated representation constructor converges too slowly, with the subsequent impact on accuracy and computational efficiency.

In this work we proved that when the domain Ω is mapped into a fully separable one \mathcal{R} standard separated constructors recover their efficiency, as the numerical results here described and discussed proved.

The technique here proposed opens numerous possibilities, such as the flow in thin ducts with rough surfaces, where fully 3D discretization fails, whereas the use of separated representations can lead to levels of resolution never attained before.

References

- [1] A. Ammar, A. Huerta, F. Chinesta, E. Cueto, A. Leygue. Parametric Solutions Involving Geometry: a Step Towards Efficient Shape Optimization. *Computer Methods in Applied Mechanics and Engineering*, 268C, 178-193, 2014.
- [2] M. Azaiez, F. Ben Belgacem, J. Casado, T. Chacon, F. Murat. A New Algorithm of Proper Generalized Decomposition for Parametric Symmetric Elliptic Problems. *SIAM Journal on Mathematical Analysis* 50(5), 5426-5445, 2018.
- [3] B. Bognet, A. Leygue, F. Chinesta, A. Poitou, F. Bordeu. Advanced simulation of models defined in plate geometries: 3D solutions with 2D computational complexity. *Computer Methods in Applied Mechanics and Engineering*, 201, 1-12, 2012.
- [4] B. Bognet, A. Leygue, F. Chinesta. Separated representations of 3D elastic solutions in shell geometries. *Advanced Modelling and Simulation in Engineering Sciences*, 2014, 1:4, <http://www.amses-journal.com/content/1/1/4>
- [5] F. Bordeu, Ch. Ghnatios, D. Boulze, B. Carles, D. Sireude, A. Leygue, F. Chinesta. Parametric 3D elastic solutions of beams involved in frame structures. *Advances in Aircraft and Spacecraft Science*, 2(3), 233-248, 2015.

- [6] F. Chinesta, A. Leygue, F. Bordeu, J.V. Aguado, E. Cueto, D. Gonzalez, I. Alfaro, A. Ammar, A. Huerta. PGD-based computational vademecum for efficient design, optimization and control. *Arch. Comput. Methods Eng.*, 20, 31-59, 2013.
- [7] F. Chinesta, R. Keunings, A. Leygue. *The Proper Generalized Decomposition for Advanced Numerical Simulations. A primer. Springerbriefs in Applied Sciences and Technology*, Springer, 2014.
- [8] F. Chinesta, A. Leygue, B. Bognet, Ch. Ghnatios, F. Poulhaon, F. Bordeu, A. Barasinski, A. Poitou, S. Chatel, S. Maison-Le-Poec. First steps towards an advanced simulation of composites manufacturing by automated tape placement. *International Journal of Material Forming*, 7(1), 81-92, 2014.
- [9] F. Chinesta, A. Huerta, G. Rozza, K. Willcox. *Model Order Reduction. Chapter in the Encyclopedia of Computational Mechanics, Second Edition*, Erwin Stein, René de Borst & Tom Hughes Edt., John Wiley & Sons Ltd., 2015.
- [10] A. Courard, D. Néron, P. Ladevèze, L. Ballere. Integration of PGD-virtual charts into an engineering design process. *Comput. Mech.*, 57, 637-651, 2016.
- [11] E. Cueto, D. González, I. Alfaro. *Proper Generalized Decompositions: An Introduction to Computer Implementation with Matlab. Springer-Briefs in Applied Sciences and Technology*, Springer, 2016.
- [12] L. Gallimard, P. Vidal, O. Polit. Coupling finite element and reliability analysis through proper generalized decomposition model reduction.

- International Journal for Numerical Methods in Engineering, 95(13), 1079-1093, 2013.
- [13] Ch. Ghnatios. Simulation avancée des problèmes thermiques rencontrés lors de la mise en forme des composites. PhD dissertation at Ecole Centrale de Nantes, 2012.
- [14] Ch. Ghnatios, F. Chinesta, Ch. Binetruy. The Squeeze Flow of Composite Laminates. International Journal of Material Forming, 8, 73-83, 2015.
- [15] Ch. Ghnatios, G. Xu, M. Visonneau, A. Leygue, F. Chinesta, A. Cimetiere. On the space separated representation when addressing the solution of PDE in complex domains. Discrete and Continuous Dynamical Systems, 9(2), 475-500, 2016.
- [16] E. Giner, B. Bognet, J.J. Rodenas, A. Leygue, J. Fuenmayor, F. Chinesta. The Proper Generalized Decomposition (PGD) as a numerical procedure to solve 3D cracked plates in linear elastic fracture mechanics. International Journal of Solid Structures, 50(10), 1710-1720, 2013.
- [17] D. Gonzalez, A. Ammar, F. Chinesta, E. Cueto. Recent advances in the use of separated representations. International Journal for Numerical Methods in Engineering, 81(5), 637-659, 2010.
- [18] T. Kolda, B. Bader. Tensor Decompositions and Applications. Society for Industrial and Applied Mathematics, 51, 455-500, 2009.
- [19] P. Ladevèze. The large time increment method for the analyze of structures with nonlinear constitutive relation described by internal variables. C. R. Acad. Sci. Paris, 309, 1095-1099, 1989.

- [20] Ladevèze, Pierre, J-C. Passieux, and David Néron. The latin multi-scale computational method and the proper generalized decomposition. *Computer Methods in Applied Mechanics and Engineering* 199(21-22), 1287-1296, 2010.
- [21] A. Leygue, F. Chinesta, M. Beringhier, T.L. Nguyen, J.C. Grandidier, F. Pasavento, B. Schrefler. Towards a framework for non-linear thermal models in shell domains. *International Journal of Numerical Methods for Heat and Fluid Flow*, 23(1), 55-73, 2013.
- [22] S. Metoui, E. Pruliere, A. Ammar, F. Dau, I. Iordanoff. The proper generalized decomposition for the simulation of delamination using cohesive zone model. *International Journal for Numerical Methods in Engineering*, 99(13), 1000-1022, 2014.
- [23] S. Perotto, M.G. Carlino, F. Ballarin. Model reduction by separation of variables: a comparison between Hierarchical Model reduction and Proper Generalized Decomposition, 2018, arXiv preprint arXiv:1811.11486.
- [24] E Pruliere. 3D simulation of laminated shell structures using the Proper Generalized Decomposition. *Composite Structures* 117, 373-381, 2014.
- [25] R. Reyes, R. Codina, J. Baiges, S. Idelsohn. Reduced order models for thermally coupled low Mach flows. *Advanced Modeling and Simulation in Engineering Sciences* , 2018, 5:1, 28.
- [26] J.P. Senecal, W. Ji. Characterization of the proper generalized decomposition method for fixed-source diffusion problems. *Annals of Nuclear Energy*, 126, 68-83, 2019.

- [27] H. Tertrais, R. Ibanez, A. Barasinski, Ch. Ghnatios, F. Chinesta. On the Proper Generalized Decomposition applied to microwave processes involving multilayered components. *Mathematics and Computers in Simulation*, 156, 347-363, 2019.
- [28] P. Vidal, L. Gallimard, O. Polit. Composite beam finite element based on the Proper Generalized Decomposition. *Computers & Structures*, 102, 76-86, 2012.
- [29] P. Vidal, L. Gallimard, O. Polit. Proper Generalized Decomposition and layer-wise approach for the modeling of composite plate structures. *International Journal of Solids and Structures*, 50(14-15), 2239-2250, 2013.
- [30] P. Vidal, L. Gallimard, O. Polit. Explicit solutions for the modeling of laminated composite plates with arbitrary stacking sequences *Composites Part B - Engineering*, 60, 697-706, 2014.
- [31] P. Vidal, L. Gallimard, O. Polit. Shell finite element based on the Proper Generalized Decomposition for the modeling of cylindrical composite structures. *Computer & Structures*, 132, 1-11, 2014.
- [32] P. Vidal, L. Gallimard, O. Polit. Assessment of variable separation for finite element modeling of free edge effect for composite plates *Composite Structures*, 123,19-29, 2015.